Supplementary Information

Regulating atomic Fe-Rh site distance for efficient oxygen reduction reaction

Tong Liu[1†], Yudan Chen[1†], Airong Xu[1], Xiaokang Liu[1], Dong Liu[1], Sicheng Li[1], Hui Huang[1], Li Xu[1], Shuaiwei Jiang[1], Qiquan Luo[2], Tao Ding[1*], & Tao Yao[1*]

[1] *National Synchrotron Radiation Laboratory, University of Science and Technology of China, Hefei 230029, P.R. China*

[2] *Institutes of Physical Science and Information Technology, Anhui University, Hefei 230601, P.R. China*

*The corresponding author
E-mail: dingtao@ustc.edu.cn; yaot@ustc.edu.cn

Experimental

Chemicals and materials

Zinc nitrate hexahydrate ($Zn(NO_3)_2 \cdot 6H_2O$, 99%), Ferric nitrate nonahydrate ($Fe(NO_3)_3 \cdot 9H_2O$, 99%), Potassium hydroxide (KOH, AR), N,N-Dimethylformamide (DMF, AR), and methanol were purchased from Sinopharm Chemical Reagent Co., Ltd. 2-methylimidazole (2-MeIm, 99%, J&K Scientific), Rhodium(III) acetylacetonate ($Rh(acac)_3$, 97%, Aladdin), Nafion (5%, Sigma-Aldrich), Graphite powder (XF078) and conductive silver paste (XFJ58) was obtained from XFNANO.

Synthesis of Fe-Rh_x@NC

In details, 0.595 g $Zn(NO_3)_2 \cdot 6H_2O$, 10 mg $Fe(NO_3)_3 \cdot 9H_2O$ and 4 mg $Rh(acac)_3$ were dissolved in a beaker A containing 30 mL methanol and sonicated for 5 mins. 1.314 g 2-methylimidazole was dissolved in a beaker B containing 10 mL methanol and sonicated for 5 mins. Then, the solution in beaker A was quickly added into beaker B and stirred at room temperature for 1 h. Then the solution was transferred into a 50 mL Teflon lined stainless-steel autoclave and sealed at 120 °C for 5 h. The product was centrifuged, washed with DMF until clear and colorless, then washed with methanol twice and dried overnight under vacuum at 60 °C. Finally, Fe-Rh_2@NC was obtained after pyrolysis at 1000 °C under N_2 atmosphere for 2 h. As comparison, The NC was also prepared with the same procedure, except for the absence of $Fe(NO_3)_3 \cdot 9H_2O$ and $Rh(acac)_3$ for NC. The Fe@NC was also prepared with the same procedure, except for the absence of $Fe(NO_3)_3 \cdot 9H_2O$. The Fe-Rh_1@NC was also prepared with the same procedure, except for the addition of 2 mg of $Rh(acac)_3$.

Characterizations

The concentration of Fe and Rh atoms was directly measured by ICP–OES (Optima 7300 DV, PerkinElmer). The X-ray diffraction (XRD) was operated on Philips X'pert PRO X-ray diffractometer with Cu Kα radiation (λ=1.5418 Å). Raman spectra were recorded on a LABRAM-HR spectrometer with a 514.5 nm Ar laser. The high-angle annular dark-field scanning transmission electron microscopy (HAADF-STEM) and corresponding electron energy loss spectroscopy (EELS) were performed on a JEOL JEM-ARF200F TEM/STEM with a spherical aberration corrector. EDS elemental mapping were obtained on a 26FEI Talos F200X device at 200 kV. XPS measurements were carried out on an ESCALAB 250Xi instrument. The binding energy scale of all measurements was calibrated by referencing C 1 s to 284.8 eV.

EXAFS experimental details. The Fe K-edge (7112 eV) XAFS spectra were carried out at the BL14W1 station of the Shanghai Synchrotron Radiation Facility (SSRF), China. The storage ring of SSRF was operated at 3.5 GeV with a maximum electron current of 250 mA. XAFS test samples are produced by mixing catalyst with graphite powder. During XAFS measurements, we calibrated the position of the absorption edge (E_0) using Fe foil. And all the XAFS data were collected during one period of beam time. The position of E_0 is defined as the point corresponding to the maximum value in the derivative curves of the XANES spectra.

Soft X-ray absorption spectroscopy measurements. The Fe L-edge XANES measurements were performed at the photoemission endstation at BL12B beamline of the National Synchrotron Radiation Laboratory (NSRL), China. The data were recorded under a total electron yield (TEY) mode with vacuum better than 5×10^{-7} Pa.

In situ SR−FTIR measurements. In situ SR−FTIR measurements were performed at the infrared beamline BL01B of the National Synchrotron Radiation Laboratory (NSRL), Chin. Using a homemade top−plate cell reflection infrared set−up with a ZnSe crystal as the infrared transmission window (cut−off energy of ~625 cm^{-1}). This end station was equipped with an FTIR spectrometer (Bruker IFS 66 v/s) with a KBr beam splitter and various detectors (herein a liquid nitrogen cooled mercury cadmium telluride detector was used) coupled with an infrared microscope (Bruker Hyperion 3000) with a ×16 objective, and could provide infrared spectroscopy measurement with a broad range of 15−4000 cm^{-1} as well as a high spectral resolution of 0.25 cm^{-1}. The catalyst electrode is connected to the wire by conductive silver adhesive. The catalyst electrode was tightly pressed against the ZnSe crystal window with a micrometre−scale gap in order to reduce the loss of infrared light. The background spectrum of the catalyst electrode was acquired at an open−circuit voltage before each systemic measurement, and the measured potential ranges of the electrocoupling reaction were 1.0 to 0.5 V.

Electrochemical measurements

The electrochemical measurements were performed in 0.1 M KOH electrolyte at room temperature using a standard three-electrode cell equipped with an electrochemical workstation (Model CHI760E, CH instruments) and a rotating ring-disk electrode (RRDE) assemble (MSR, Pine Research Instrumentation, USA). A rotating disk electrode (RDE) or RRDE of 5mm in diameter loaded with the catalyst ink was used as working electrode. A graphite rod was chosen as the counter electrode and Ag/AgCl electrode (3 M KCl) was used as the reference electrode. Approximate 5 mg of the catalysts were ultrasonically dispersed in 1 mL of 1:1 (volume ratio) deionized water and isopropanol mix solvent with 25 μL of Nafion solution (5 wt%). Then, 15 μL of homogeneous ink was dropped onto the working electrode and then fully dried at room temperature. to achieve a 0.4 mg cm^{-2} loading amount. The RDE/ RRDE tests were measured at various rotating speed from 400 to 2500 rpm in O_2-saturated 0.1 M KOH aqueous solution with a sweep rate of 20 mV/s. All potentials were calibrated versus RHE: E (RHE) = E (Ag/AgCl) + 0.197 V + 0.0592 × pH. Cyclic voltammetry (CV) ranging from 10 to 100 mVs^{-1} was conducted to calculate the double layer capacitance (C_{dl}).

The number of electrons transferred and the H_2O_2 yield were evaluated from RRDE measurements using the following equations:

Number of electron transfer (n) during ORR:

$$n = 4 \times \frac{I_d}{I_d + \frac{I_r}{N}} \quad (1)$$

Percentage of peroxide $H_2O_2(\%)$ during the ORR tests:

$$H_2O_2(\%) = 200 \times \frac{I_r}{I_d \times N + I_r} \quad (2)$$

where I_d and I_r are disk and ring current densities, respectively, and N is the current collection efficiency of the Pt ring which is 0.37.

The electron transfer number (n) and kinetic current density (J_k) of ORR from RDE can be determined on the basis of the Koutechy-Levich equation:

$$\frac{1}{J} = \frac{1}{J_L} + \frac{1}{J_K} = \frac{1}{B\omega^{\frac{1}{2}}} + \frac{1}{J_K} \quad (3)$$

$$B = 0.62nFC_0D_0^{\frac{2}{3}}V^{-\frac{1}{6}} \quad (4)$$

Where J is the current density obtained from the ORR measurement, J_K and J_L are the kinetic and limiting current densities, n is the electron transfer number, ω is the angular velocity of the disk, F is the Faraday constant (96485 C mol^{-1}), C_0 is the bulk concentration of O_2 (1.2×10^{-6} mol cm^{-3}), D_0 is the diffusion coefficient of O_2 in 0.1 M KOH solution (1.9×10^{-5} cm^2 s^{-1}), and V is the kinematic viscosity of the electrolyte (0.01 cm^2 s^{-1}).

DFT calculations

The calculations were performed within the Density Functional Theory (DFT) framework implanted in Vienna ab initio Simulation Package (VASP) **[1]**. The interaction between ions and electrons was described in the Projector Augmented Wave (PAW) Method **[2]**. The electron exchange and correlation energy were described using the generalized gradient approximation-based Perdew–Burke–Erzenhorf (PBE) functional **[3]**. The semi-empirical London dispersion corrections of Grimme and colleagues (DFT-D3) were conducted to calculate the interactions between absorbers and slabs **[4]**. The models of Fe-N_4, FeRh-N_6, Fe-N_4/Rh-N_4-1, Fe-N_4/Rh-N_4-2, and Fe-N_4/Rh-N_4-3 with a 9 × 9 × 1 graphene monolayer supercell were chosen for the calculation. and all the atoms were fully relaxed during the calculations. A sufficiently large vacuum region of 15 Å was used for all the models to ensure the periodic images were well separated. the Brillouin-zone integrations were carried out using Monkhorst-Pack grids of special points. A gamma-centered (2 × 2 × 1) k-point grid was used for all the models. To obtain the accurate structure, The plane-wave cutoff energy was set up to 500 eV. The force convergence was set to be <0.02 eV $Å^{-1}$, and the total energy convergence was set to be $<10^{-5}$ eV. The free energy of the adsorbed state was calculated as follows based on the adsorption energy:

$$\Delta G_* = \Delta E_* + \Delta E_{ZPE} + U_{(T)} - T\Delta S \quad (5)$$

where ΔE* is the adsorption energy directly obtained from DFT calculations, ΔE_{ZPE} is the zero-point energy, $U_{(T)}$ is the heat capacity correction energy, and T is the temperature (T = 298.15 K), ΔS is the change in entropy. Herein, the Gibbs energy is corrected by using the VASPKIT code **[5]**.

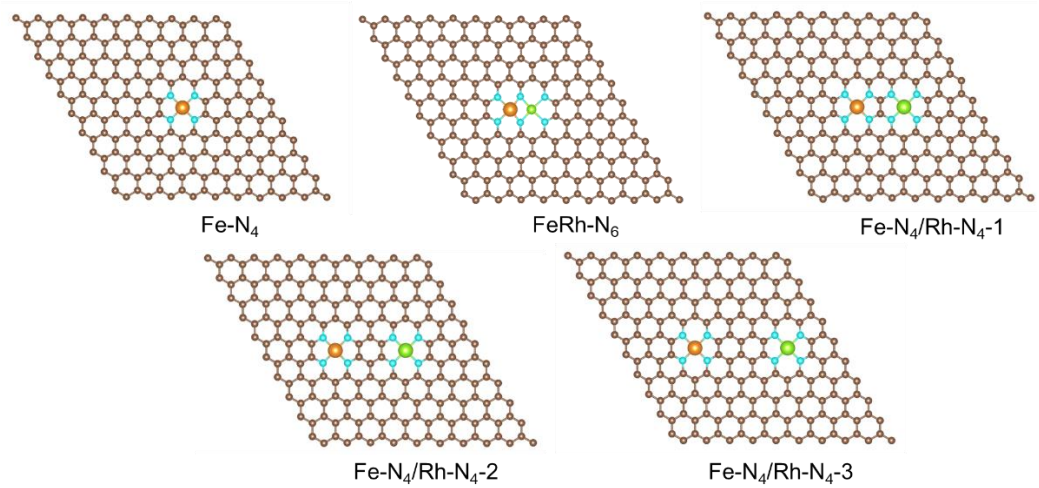

Figure S1. The atomic calculated models of Fe-N_4, FeRh-N_6, Fe-N_4/Rh-N_4-1, Fe-N_4/Rh-N_4-2, and Fe-N_4/Rh-N_4-3. (light blue, brown, orange and green balls represent N, C, Fe and Rh atoms, respectively).

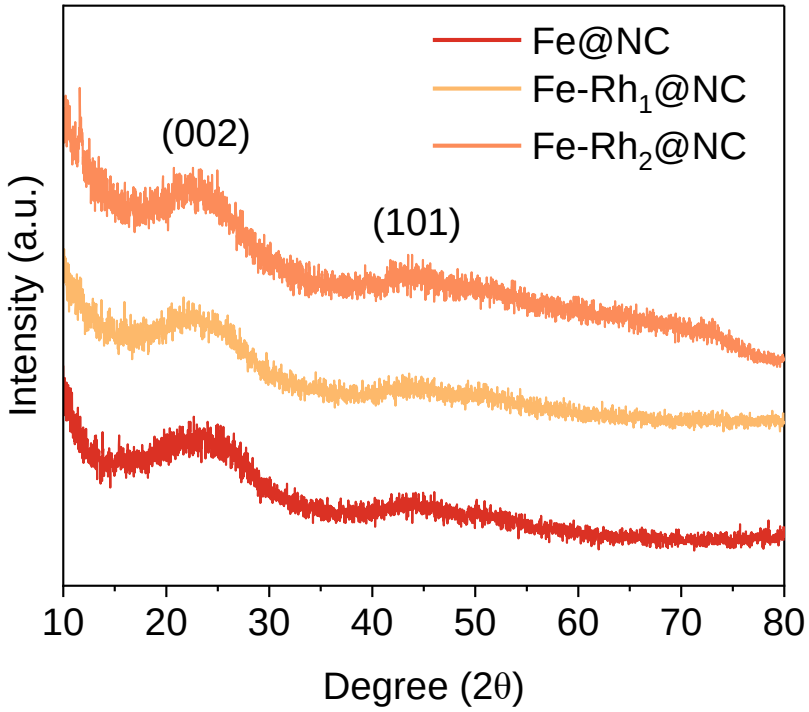

Figure S2. XRD patterns of Fe@NC, Fe-Rh_1@NC, and Fe-Rh_2@NC.

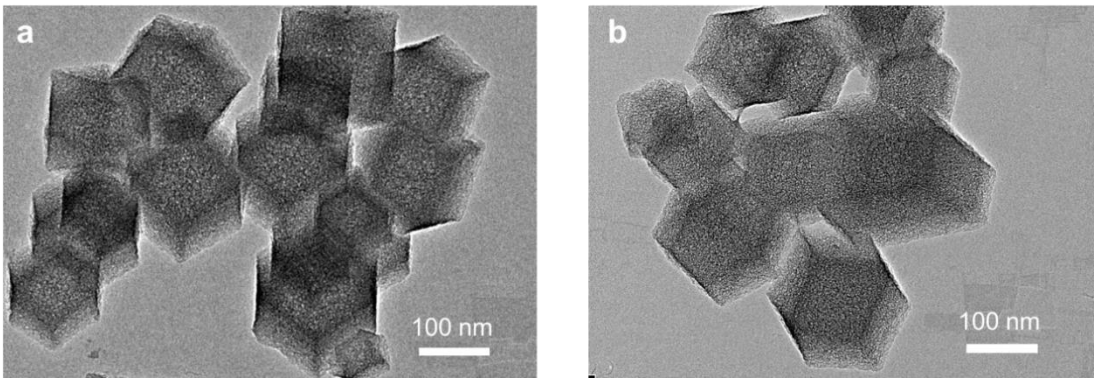

Figure S3. TEM images of Fe@NC and Fe-Rh_1@NC.

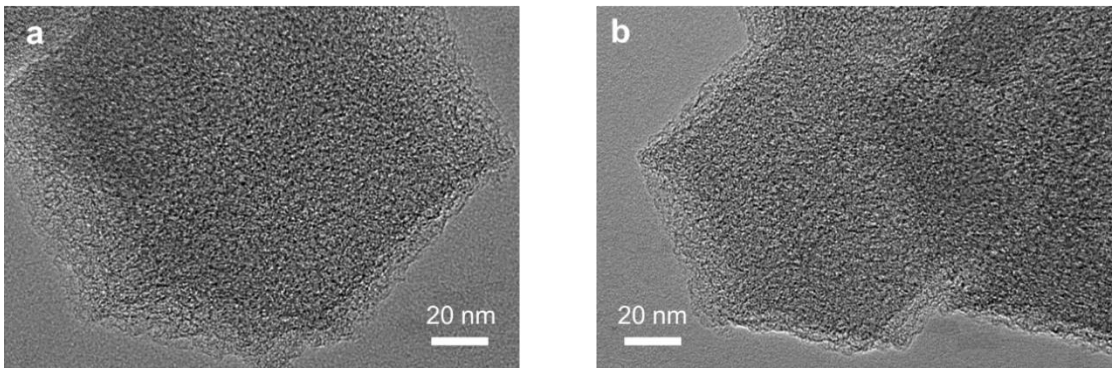

Figure S4. HRTEM images of Fe@NC and Fe-Rh_1@NC.

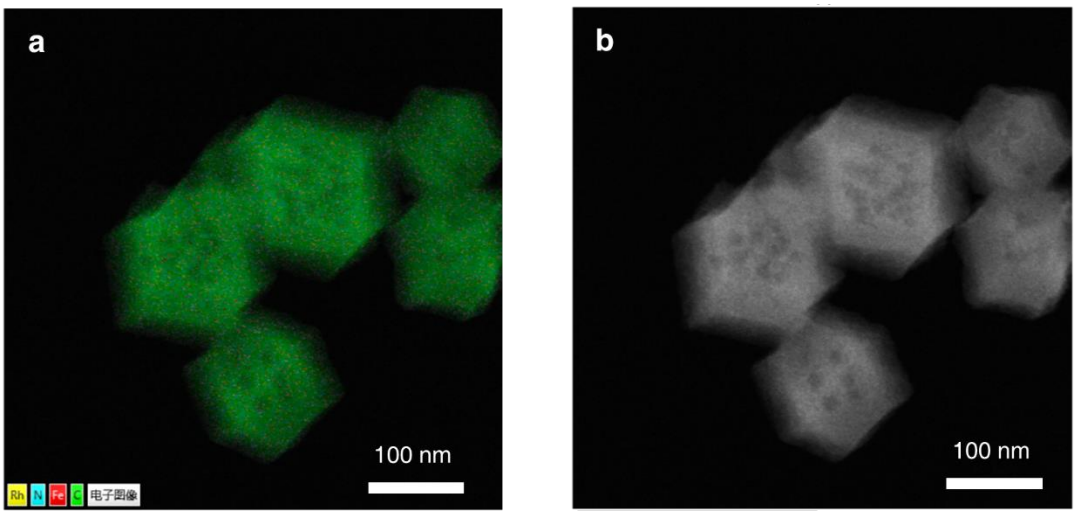

Figure S5. The EDS layered images of Fe-Rh_2@NC.

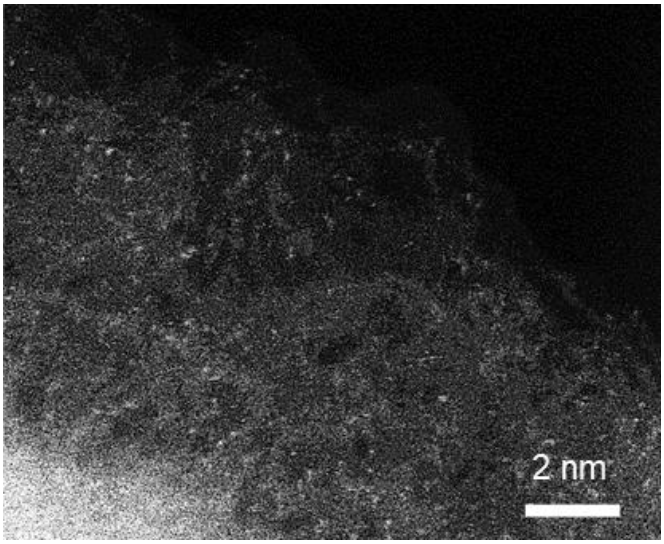

Figure S6. HAADF-STEM image of Fe@NC.

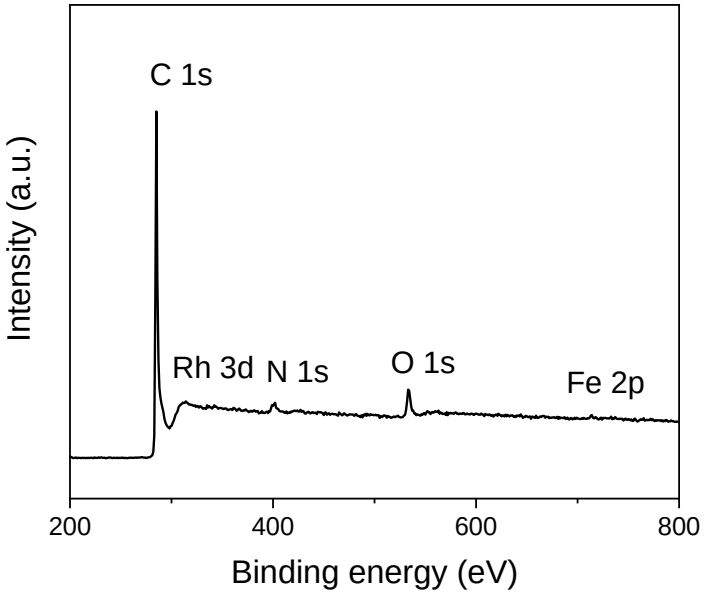

Figure S7. Survey scan of Fe-Rh_2@NC.

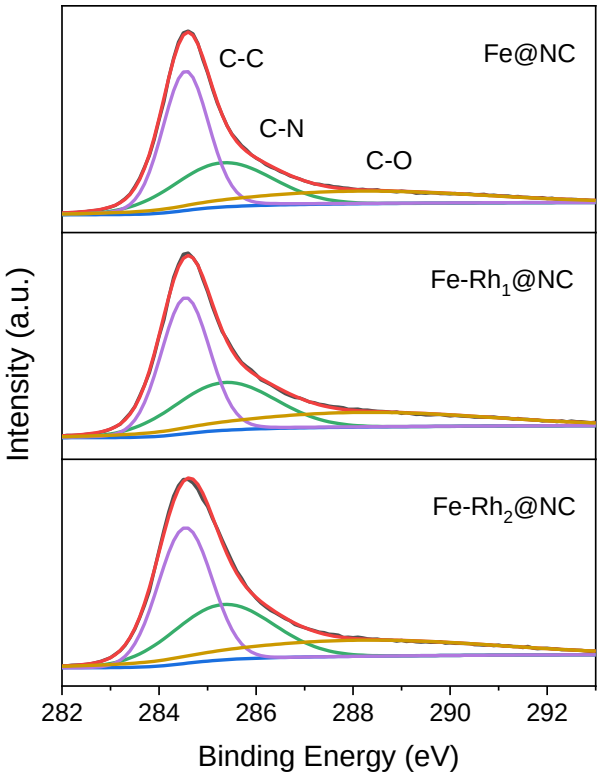

Figure S8. High resolution C 1s XPS spectra of Fe-Rh_x@NC.

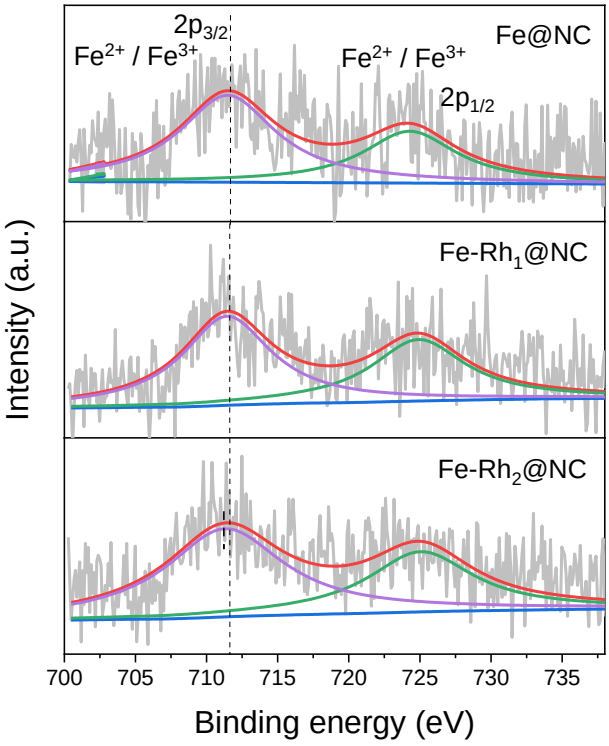

Figure S9. High resolution Fe 2p XPS spectra of Fe-Rh$_x$@NC.

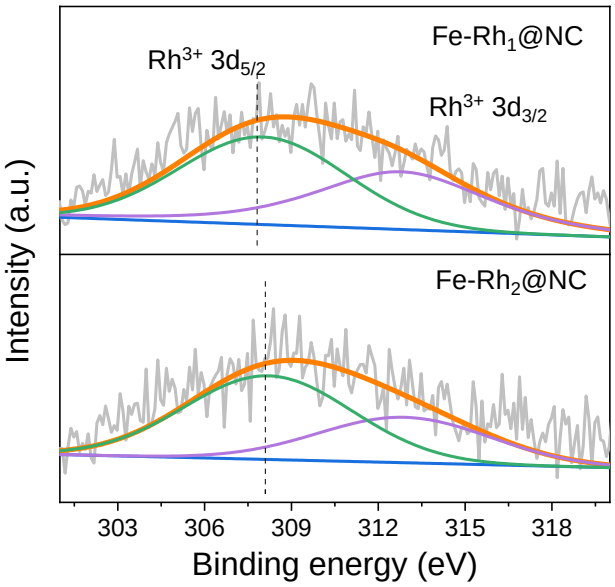

Figure S10. High resolution Rh 3d XPS spectra of Fe-Rh$_x$@NC.

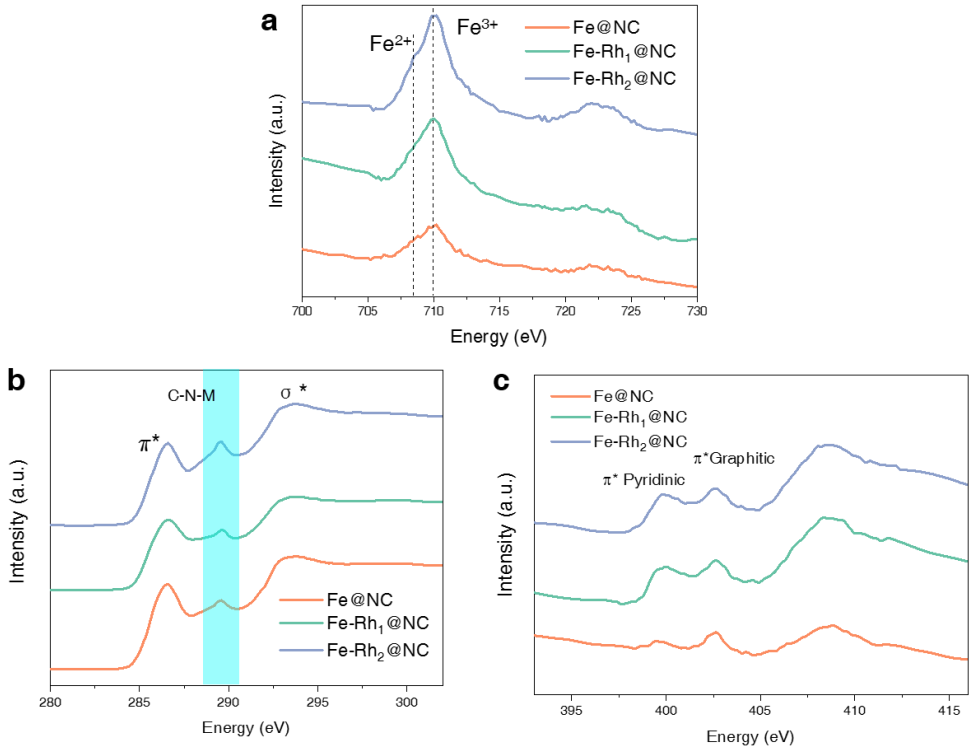

Figure S11. Chemical state and atomic local structure. (a) Fe *L*-edge. (b) C *K*-edge, and (c) N *K*-edge soft XANES spectra of Fe-Rh$_x$@NC.

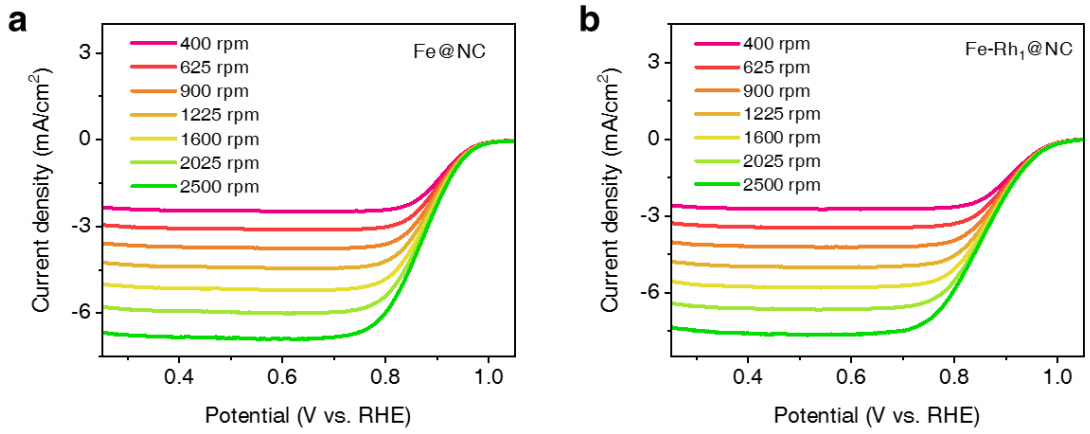

Figure S12. LSV curves of (a) Fe@NC and (b) Fe-Rh$_1$@NC at various rotation rates.

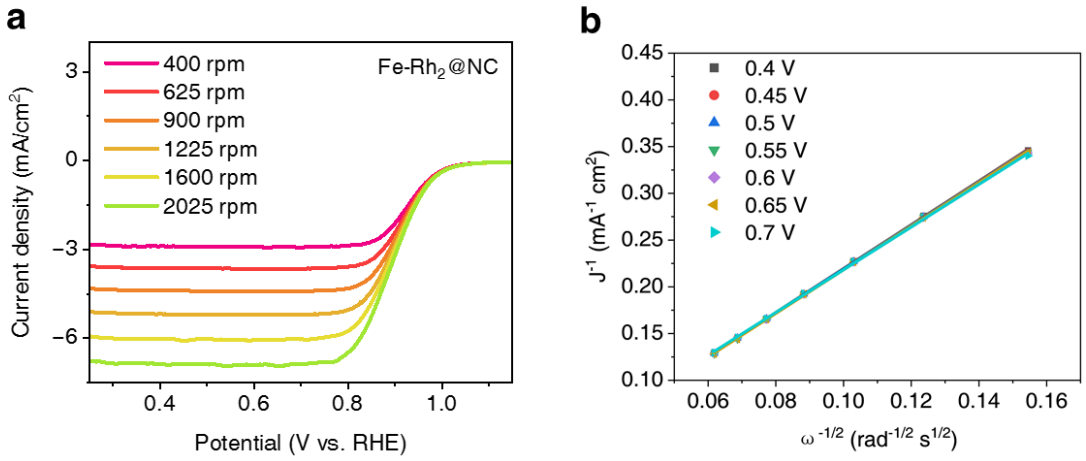

Figure S13. (a) LSV curves of Fe-Rh2@NC at various rotation rates. (b) The Koutecky–Levich plots of Fe-Rh2@NC samples.

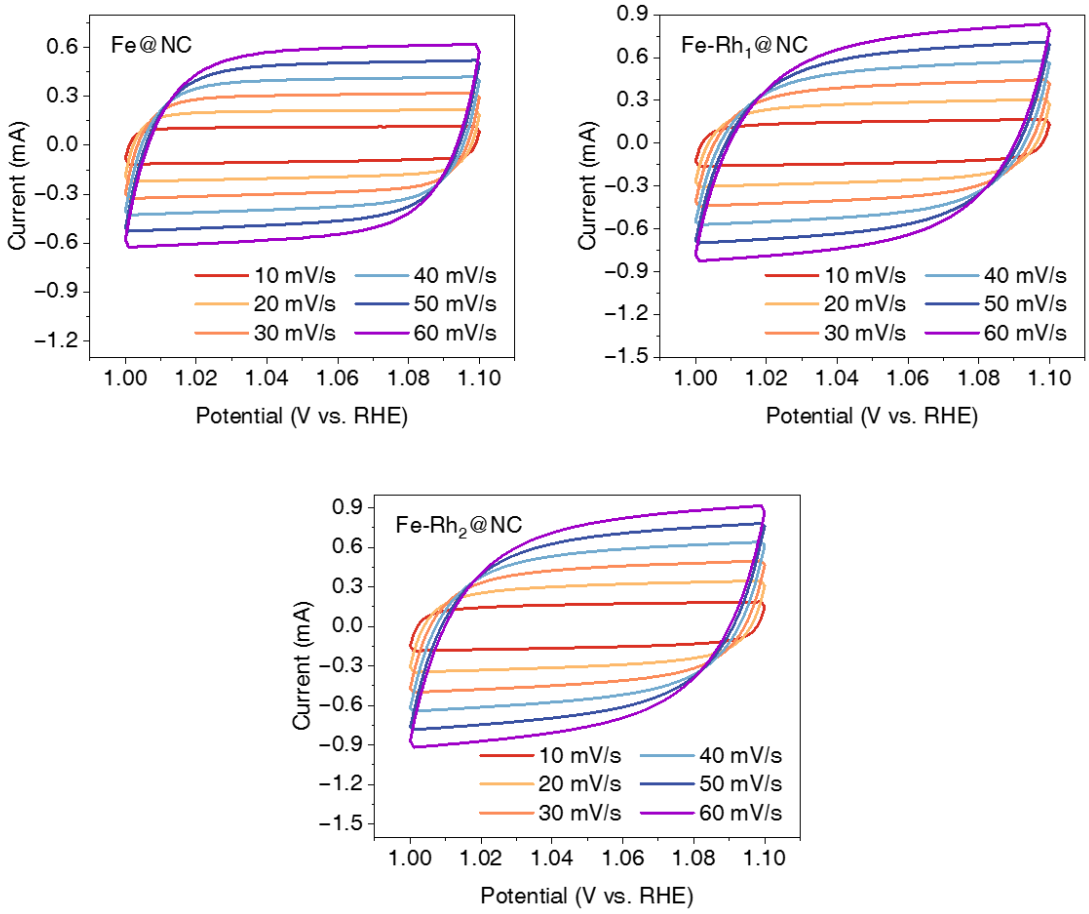

Figure S14. The CV curves of Fe-Rhx@NC electrocatalyst obtained at different scan rates.

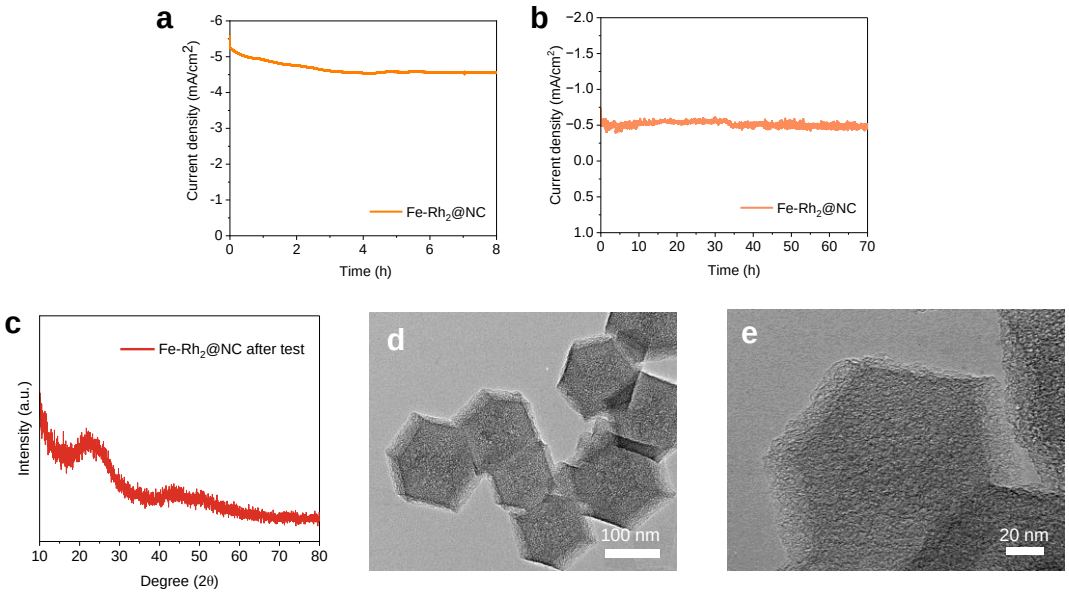

Figure S15. (a) I-t curves at 0.7 V at a rotation speed of 1600 rpm in O_2-saturated 0.1 M KOH of Fe-Rh_2@NC. (b) I-t curves at 0.7 V without rotation in O_2-saturated 0.1 M KOH of Fe-Rh_2@NC. (c) XRD pattern, (d) TEM, and (e) High-resolution TEM image of Fe-Rh_2@NC catalyst after ORR stability test.

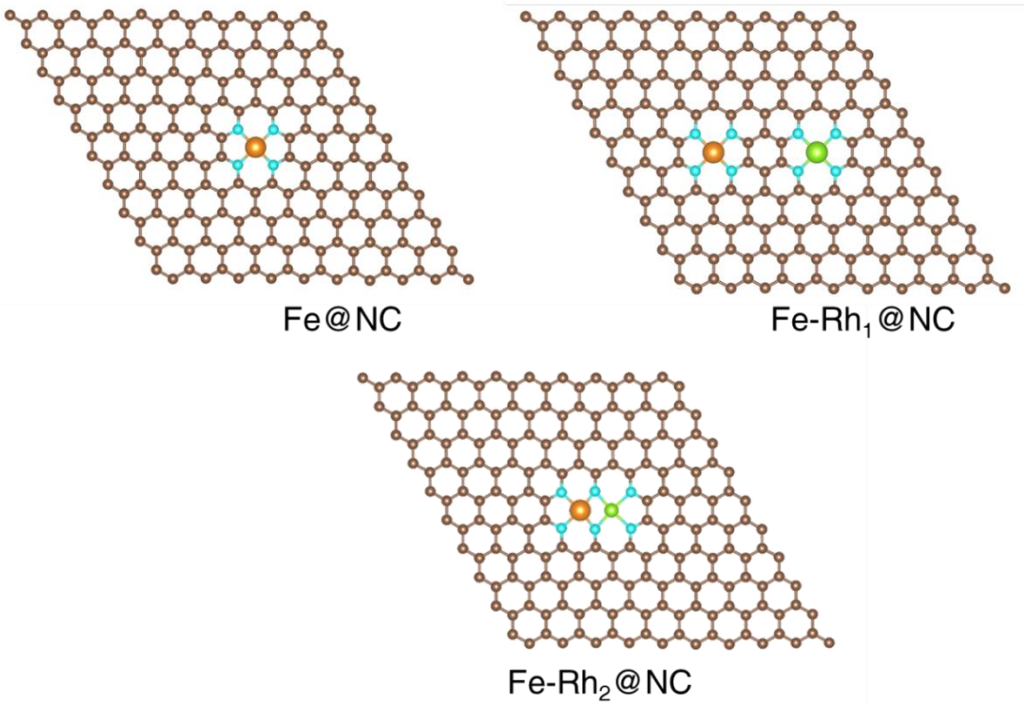

Figure S16. The atomic calculated models of Fe-Rh_x@NC (light blue, brown, orange and green balls represent N, C, Fe and Rh atoms, respectively).

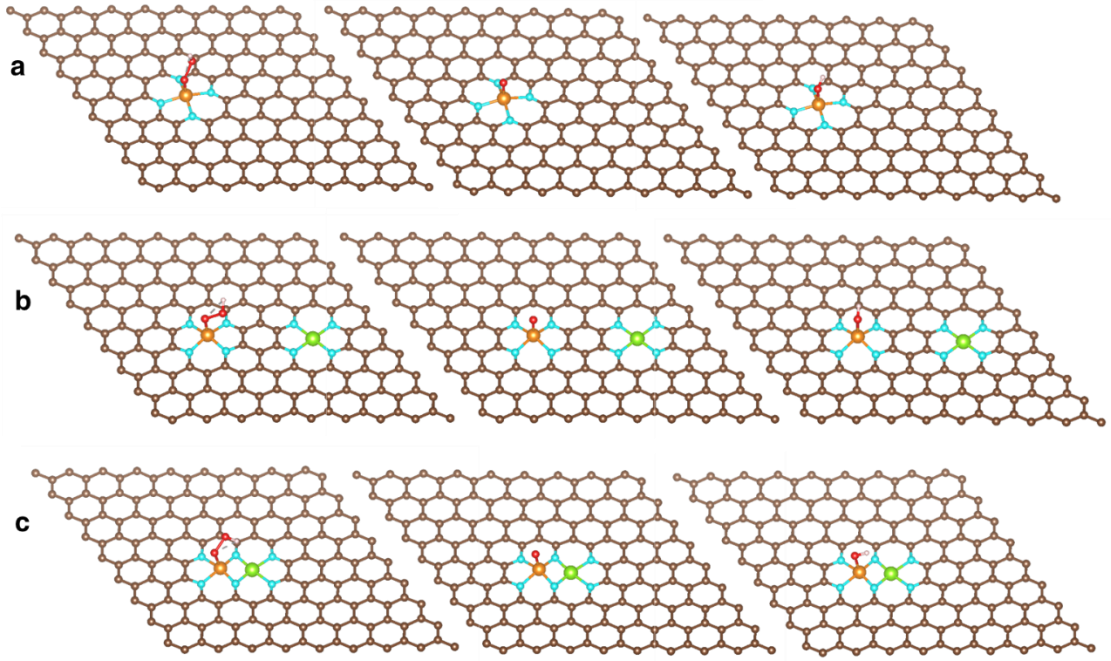

Figure S17. The atomic models of ORR reaction process of (a) Fe@NC, (b) Fe-Rh_1@NC, and (c) Fe-Rh_2@NC. (brown, light blue, red, pink, orange and green balls represent C, N, O, H, Fe and Ru atoms, respectively).

Table S1. The content of Fe (wt%) and Rh (wt%) examined by ICP–MS.

	Fe@NC	Fe-Rh_1@NC	Fe-Rh_2@NC
Fe (wt%)	1.31%	0.94%	1.06%
Rh (wt%)	-	0.3%	0.7%

Table S2. The elements atomic content percentage by XPS.

	C (Atomic %)	N (Atomic %)	Fe (Atomic %)	Rh (Atomic %)
Fe@NC	95.28	4.28	0.45	-
Fe-Rh_1@NC	92.02	6.86	0.47	0.65
Fe-Rh_2@NC	94.47	4.31	0.41	0.8

Table S3. EXAFS curve fitting parameters of the Fe *K*-edge.

Sample	Path	CN	R (Å)	σ^2 (10^{-3}Å^2)	ΔE_0 (eV)
FeN	Fe-N	4.1	1.99	5.2	-2.2
$FeRh_1$	Fe-N	4.1	1.99	5.1	-2.0
$FeRh_2$	Fe-N	4.3	1.99	5.3	-2.1

Table S4. Comparison table of electrocatalysts ORR performance of Fe-based catalyst.

Electrocatalysts	Electrolyte	$E_{1/2}$ (V vs RHE)	Ref.
Fe-Rh_2@NC	0.1 M KOH	0.91	This work
FeCo-NCH	0.1 M KOH	0.89	Nat. Common. 2023, 14:1822
FeNC-1200	0.1 M $HClO_4$	0.80	Adv. Mater. 2023, 35, 2204474
Fe-SAC	0.1 M KOH	0.90	Nano Res. 2022, 15, 1966–1972
SA-Fe-NGM	0.5 M H_2SO_4	0.83	J. Am. Chem. Soc. 2022, 144, 9280−9291
Fe–N/C-SAC	0.1 M KOH	0.91	Adv. Funct. Mater. 2022, 32, 2108345
Fe–N_4-PN	0.1 M KOH	0.91	ACS Catal. 2021, 11, 6304-6315
Fe_{SA}/Fe_{AC}−2DNPC	0.5 M H_2SO_4	0.81	Nat. Common. 2022, 13:2963
Fe–N/S–C	0.1 M KOH	0.88	Small, 2022, 18, 2106568
FePNC	0.5 M H_2SO_4	0.76	Adv. Energy Mater. 2023, 2301223
FePNC	0.1 M KOH	0.90	Adv. Energy Mater. 2023, 2301223
$FeMn_{ac}$/Mn-N_4C	0.5 M H_2SO_4	0.79	Angew. Chem. Int. Ed. 2022, e202214988
$FeMn_{ac}$/Mn-N_4C	0.1 M KOH	0.90	Angew. Chem. Int. Ed. 2022, e202214988

Reference:

[1] G. Kresse av, J F. *Phys Rev B*, 1996, 54: 11169–11186.

[2] Blöchl P E. *Phys Rev B*, 1994, 50: 17953-17979.

[3] John P. Perdew, Kieron Burke, Ernzerhof M. *Phys. Rev. Lett.*, 1996, 77: 3865–3868.

[4] Grimme S. *J Comput Chem*, 2006, 21: 1787-1799.

[5] Wang V, Xu N, Liu J-C, Tang G, Geng W-T. *Comput Phys Commun*, 2021, 267: 108033.